Geophysical Journal International

Geophys. J. Int. (2019) **218,** 190–199
Advance Access publication 2019 March 27
GJI Seismology

doi: 10.1093/gji/ggz149

Topography of the western Pacific LLSVP constrained by *S*-wave multipathing

Sunil K. Roy,[1,2] Nozomu Takeuchi,[1] D. Srinagesh,[2] M. Ravi Kumar[2,3] and Hitoshi Kawakatsu[1]

[1]*Earthquake Research Institute, University of Tokyo, Tokyo* 1130032*, Japan. E-mail: ssunilroy@gmail.com*
[2]*CSIR-National Geophysical Research Institute, Hyderabad* 500007*, India*
[3]*Institute of Seismological Research, Gandhinagar* 382009*, India*

Accepted 2019 March 20. Received 2019 March 15; in original form 2018 August 6

SUMMARY

We found that SH_{diff} phases generated by earthquakes in the Fiji–Tonga, recorded in India, are accompanied by secondary pulses. We interpreted them as a consequence of multipathing of *S* waves caused by the Pacific large low-shear-velocity province (LLSVP). We analysed the differential traveltimes between SH_{diff} and the secondary pulse, together with the absolute SH_{diff} arrival times, to constrain the thickness and velocity perturbations in the western end of the Pacific LLSVP. Our preferred model shows a lateral variation in the thickness of the LLSVP; the southern part reveals a thicker (300 km) low-velocity region compared to the northern part (200 km). However, the velocity perturbations of the LLSVP appear to be comparable (−1.5 per cent). The results are consistent with a scenario that the LLSVP is a chemically distinct pile with significant surface topography.

Key words: Mantle processes; Pacific Ocean; Body waves; Wave scattering and diffraction; Dynamics: convection currents, and mantle plumes.

1 INTRODUCTION

It is now established that two large low-shear-velocity provinces (LLSVPs) exist in the lowermost mantle beneath the Pacific and Africa. Their overall geometry is constrained by both global (e.g. Dziewonski 1984; Tanimoto 1990; Su & Dziewonski 1991; Woodward & Masters 1991; Ritsema *et al.* 1999; Becker & Boschi 2002; Takeuchi 2007, 2012; Lekic *et al.* 2012) and regional array studies (e.g. Ritsema *et al.* 1998; Ni & Helmberger 2003; He *et al.* 2006; Wang & Wen 2007; He & Wen 2012). Owing to the higher bulk sound velocities (e.g. Su & Dziewonski 1997; Masters *et al.* 2000; Koelemeijer *et al.* 2016), higher densities (e.g. Ishii & Tromp 1999; Trampert *et al.* 2004), sharp edges (e.g. Ni *et al.* 2002; To *et al.* 2005; Takeuchi *et al.* 2008; Sun *et al.* 2009; Frost & Rost 2014) and possible presence of sharp top surfaces (e.g. Sun & Miller 2013; Zhao *et al.* 2015), the LLSVPs have often been postulated to be chemically distinct from the ambient mantle (e.g. Tackley 2002, 2013).

It is now widely accepted that the height of the African LLSVP exceeds 1000 km in a cross-sectional view through its southern and eastern ends (e.g. Ritsema *et al.* 1998; Ni & Helmberger 2003; Wang & Wen 2007). Although the stability of such large-scale anomalies was debated in the context of mantle dynamics (Davaille 1999; Tan & Gurnis 2005), several studies have succeeded in generating synthetic 3-D models that explain the major features of seismological observations (e.g. McNamara & Zhong 2005; Bull *et al.* 2009). However, after the discovery of the post-perovskite phase (Murakami *et al.* 2004), some studies interpret these features by invoking thermal anomalies alone, considering the topography of the D″ discontinuity and the contrast in material properties between perovskite and post-perovskite (e.g. Bull *et al.* 2009; Davies *et al.* 2012). In these studies, the LLSVPs are assumed to be plume clusters blurred by the limited resolution of the tomographic images (Schubert *et al.* 2004) rather than thermochemical piles. It appears that the origin of LLSVPs continues to be a matter of debate.

To constrain the origin, deciphering the detailed geometry of the LLSVPs would be useful. The height of the African LLSVP is suggested to be shorter (∼600 km) at its western edge (Sun & Miller 2013). However, the other details are not well constrained. Also, the height of the Pacific LLSVP is less constrained due to the inadequate coverage of the relevant seismic rays. Existence of small-scale variations inside the Pacific LLSVP was suggested based on an abrupt change in the observed traveltimes (e.g. Takeuchi & Obara 2010; He & Wen 2012; Tanaka *et al.* 2015). However, it is not straightforward to identify whether such variations are caused by the geometry of the LLSVP or volumetric heterogeneities within. Although results from global tomography suggested that the height of the Pacific LLSVP is generally shorter (∼300 km) than that of the African LLSVP (e.g. Takeuchi 2007, 2012), detailed analyses of regional array data have suggested significant regional variations (e.g. Takeuchi *et al.* 2008; He & Wen 2009, 2012).

In order to further constrain the geometry of the LLSVPs, new techniques and observations would be critical. To decipher the detailed structure of the lower mantle, analysis of the discrepancies in splitting of shear waves like *S-ScS* and *SKS-SKKS* (e.g. Kendall & Silver 1996; Lynner & Long 2014; Roy *et al.* 2014; Long & Lynner 2015), waveforms of turning (e.g. PKP and Pdiff) and reflected ray phases (e.g. *ScS*, *PcP*; e.g. Garnero 2000) is extensively conducted. In this study, we focus on mulitipathing of *SH* waves recorded by an array in India. We analyse the SH_{diff} phase and its post-cursor to investigate the topography at the western edge of the Pacific LLSVP. This region is ideally suited for applying this technique because it is well sampled by *ScS* waves (see e.g. fig. 2 of He & Wen 2009) and the boundary location of the LLSVP, one of the critical parameters in this analysis, has been tightly constrained (see e.g. fig. 8 of French & Romanowicz 2014). For models with a low-velocity zone (LVZ), we expect the arrivals of prograde and retrograde branches of direct waves to be registered at a single station. In the distance range of waveforms used in this study (102°–115°), we usually expect SH_{diff} to be the direct phase. However, in the presence of an LVZ in the lowermost mantle, with appropriate velocity reduction and thickness, we also expect bottoming of the *S* wave, inside it (Supporting Information Fig. S1). In this study, we have used the differential traveltime between SH_{diff} and *SH*, together with the differential apparent velocity, to constrain the thickness of the LVZ (i.e. LLSVP). We apply this approach to data recorded by the broad-band seismograph array operated by the CSIR-National Geophysical Research Institute (NGRI), Hyderabad, India. These data have been previously used for studies on the lowermost mantle anisotropy and core–mantle boundary (CMB) structures, through analysis of *SK(K)S* and *ScS* phases, respectively (Rao & Kumar 2014; Roy *et al.* 2014). However, the SH_{diff} waveforms have not been analysed yet, and the maiden use of this data set therefore provides new information.

2 DATA AND OBSERVATIONS

In total, data from 49 stations in the Indian sub-continent are used in this study (Supporting Information Table S1, Fig. 1). Description of the station configuration and deployment is provided in earlier articles dealing with shear wave anisotropy of the Indian continent (Roy *et al.* 2012, 2014, 2016). Many of these stations are aligned in the north–south direction, around 80°E, and, for later discussions, we classify the array into the northern and southern arrays (the magenta and dark green triangles, respectively, in Fig. 1). The SH_{diff} phase generated by earthquakes in the Fiji–Tonga subduction zone samples a portion of the western edge of the Pacific LLSVP (solid lines in Fig. 1). A systematic observation of the SH_{diff} phase enabled us to examine the signature of the western edge of the Pacific LLSVP. To test the existence of a secondary pulse in each trace, we applied a two-pole Butterworth bandpass filter in the range of 3.2–32 s to the displacement waveforms of earthquakes having depths >100 km and $M > 5.5$, from the Fiji–Tonga slab. We did not observe any secondary pulses in the waveforms corresponding to shallow earthquakes. However, we chose to ignore the data of shallow earthquakes, since they are more complex and may suffer from phase overlapping due to interference with depth phases. While picking the arrival time of a pulse, we applied a two-pole Butterworth bandpass filter of 3.2–12.5 s to the velocity waveforms, because displacement seismograms often suffer from phase overlapping that blurs the peak location of the secondary pulse. The corner frequencies are empirically chosen to maximize the peak amplitudes of the secondary pulses.

A record section of the SH_{diff} phase from the Fiji–Tonga region shows the arrival of a second phase adjacent to it (Figs 2a and b). In order to further authenticate the secondary pulses, we also present the displacement waveforms (Supporting Information Fig. S2). The sections are made with respect to azimuth (Fig. 2a) and distance (Fig. 2b). The secondary pulses are more coherent in Fig. 2(a) than in Fig. 2(b), which suggests the existence of azimuthally dependent structures. The second pulse has larger amplitudes on the northern array (with larger azimuths) than those on the southern array. On an average, the arrival time of the second pulse relative to the initial pulse is more advanced on the northern array. There are 28 deep (>100 km) events from the Fiji–Tonga slab for which SH_{diff} could be confirmed. Qualitative inspection of the waveforms from these events resulted in the selection of five events, which are assigned alphabetic names (Table 1), in which the second pulse is well identified as an isolated packet (Fig. 2 and Supporting Information Fig. S2). The remaining 23 events are not selected, because either the waveforms are too noisy or the SH_{diff} pulse is so broad that it overlaps with the second pulse.

For the selected events, we pick the peak time of the first and second pulses within the SH_{diff} window in the velocity seismogram. The second pulse is consistently well observed in the northern array, whereas it is sometimes difficult to identify it in the case of the southern array. We obtained 54 observations for the first and second pulses, in the distance range of 102.0° to 115.1°. The observed relative arrival time of the second pulse with respect to the first pulse varies from 3.85 to 11.17 s. To illustrate the sampling region, the vertical cross-section including event B and station KLR (shown in Fig. 1), superimposed on the tomography model of Takeuchi (2012), is shown in Fig. 3(a). The differential traveltimes show systematic variations when plotted at the entry point of the SH_{diff} phase at the CMB (Fig. 4). The differential times get larger when the ray samples the southern region. These times also get larger when the entry point is located to the east and the ray travels a longer distance in the lower velocity region. However, such a tendency gets weaker for the data sampling the northern region. The observed amplitude of the secondary pulse is 32 per cent to 95 per cent of the SH_{diff} pulse.

Fig. 5 shows the observed relative traveltimes as a function of distance. In many studies, the distance is normalized to the source at the surface. However, in this study, we prefer not to follow that approach because the ray is influenced more strongly by the distance between the source and the side boundary, compared to the event depth. Indeed, even if we normalize the distance in a conventional manner, the distance is shifted by less than 1°, which will not essentially affect the discussions below. We modelled the observed traveltimes (shown by thick green bars) by the regression line in the form of $\delta t = a(\Delta - 100^\circ) + b$, where Δ is the distance and δt is the differential traveltime. The estimated values are $a = 0.10 \pm 0.05$ and $b = 4.84 \pm 0.47$ for the northern array and $a = 0.31 \pm 0.08$ and $b = 4.78 \pm 0.71$ for the southern array. We observe significant differences in the slope, which suggest structural variations in the azimuthal direction.

3 INTERPRETATION

The cross-section of Fig. 3(a) shows that the SH_{diff} phase samples the region with strong low-velocity anomalies associated with the Pacific LLSVP, traverses the western edge and pierces through

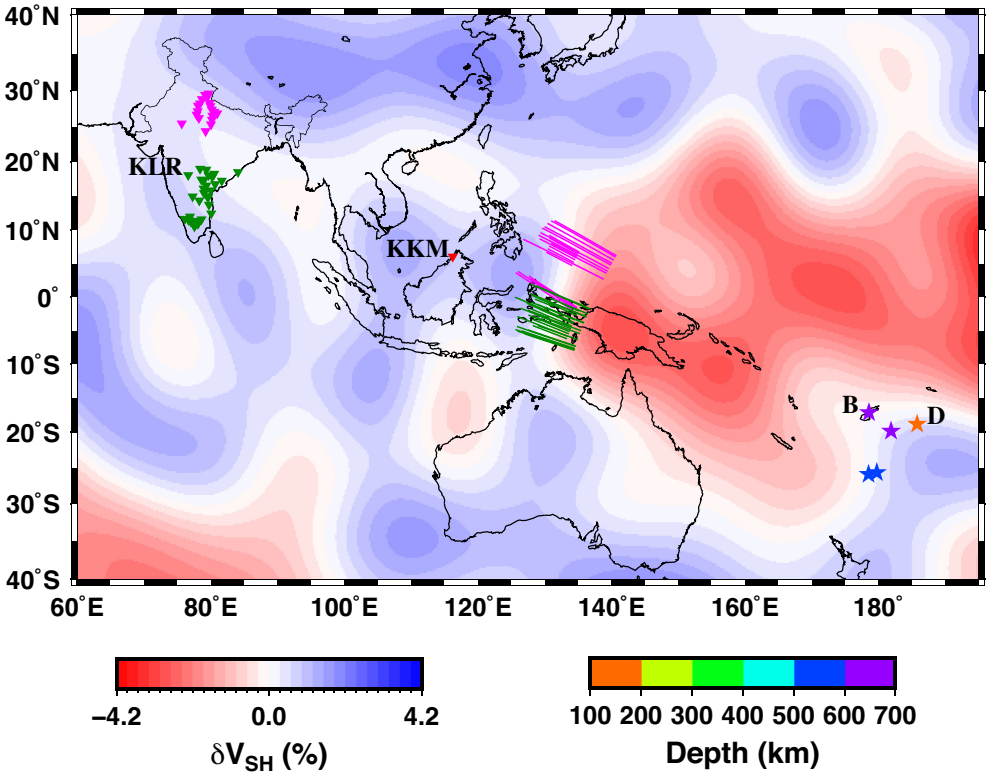

Figure 1. Source–receiver geometry of our data set for the five deep earthquakes from the Fiji–Tonga slab (filled star) and the Indian seismic array (inverse triangle). The colour of the stars denotes the source depth, and magenta and dark green triangles indicate the stations belonging to the northern and southern array, respectively. The magenta and dark green lines demarcate a ray segment of SH_{diff} phase on the CMB for the northern and southern seismic array, respectively. The background colour represents the shear wave velocity variation in the lowermost mantle in the model SH18CE (Takeuchi 2012). The locations of station KLR, event B and event D (see the text for details) are also shown. The red triangles denote the locations of reference stations (whose waveforms are shown in Supporting Information Fig. S2).

the slightly higher velocity region. We interpret that the second pulse is generated from the lowermost mantle structure because of the following four reasons. (1) The possibility of a source side structure is small, since we did not observe a second pulse in the direct SH phase, for the same event recorded at closer distances in Southeast Asia (Supporting Information Fig. S2). (2) In a similar fashion, the possibility of receiver side structure is small, since we did not observe the pulse for events at closer distances. (3) The observed amplitude of the secondary pulse is 32–95 per cent of that of the direct wave, and such a larger amplitude is not likely except for the mulitpathing or post-critical reflection. (4) The Pacific LLSVP is the most pronounced feature in the cross-section of Fig. 3(a), and the LVZ above the CMB can generate multipathing (Supporting Information Fig. S1); also, the differential traveltimes between the first and second pulses are correlated with the LLSVP geometry (Fig. 4). We interpret the second phase to be the direct SH wave that samples the top edge of the LLSVP and then gets refracted (or diffracted) before reaching the receiver (Fig. 3b).

We think it is unlikely that the secondary pulses are caused by random scattering or refraction traversing far outside of the great-circle plane. A plot of the displacement seismograms confirms that the secondary pulses gradually change with azimuth (Fig. 2 and Supporting Information Fig. S2). It intuitively implies that random scattering is unlikely to be the cause. Typically, the differential traveltime between the first and second pulses is ∼5 s. Considering the possible locations of point scatterers for a differential traveltime of 5 s on the CMB, the seismic ray of the secondary pulse will not traverse more than ∼500 km from the great-circle plane.

Besides the volumetric heterogeneities, anisotropy can be another candidate to produce multipathing. Indeed, several studies suggested the existence of azimuthal anisotropy in the vicinity of LLSVPs (e.g. Wang & Wen 2007; Cottaar & Romanowicz 2013; Lynner & Long 2014; Ford *et al.* 2015; Creasy *et al.* 2017) and another lower velocity province on the CMB (Perm Anomaly; e.g. Long & Lynner 2015). However, these studies suggested anisotropy outside the low-velocity provinces rather than inside. Considering the differential traveltimes are likely to be related to the LLSVP structure (Fig. 4), anisotropy is unlikely to be the major cause of the multipathing. We therefore ignore these effects in the following modelling.

4 MODELLING

We search for a model that best explains the observed traveltimes. Because the observed waveforms are highly azimuthally dependent, we need to search for an azimuthally dependent structural model. Also, since the observed waveforms in Fig. 2(a) show that the amplitude and traveltime of the secondary pulse gradually change from the southern to the northern array, we probably need a 3-D model with gradual azimuthal variations. However, since the computation of synthetic seismograms incorporating 3-D models requires huge computational resources, we search for 2-D models to explain the data from northern and southern arrays separately, to

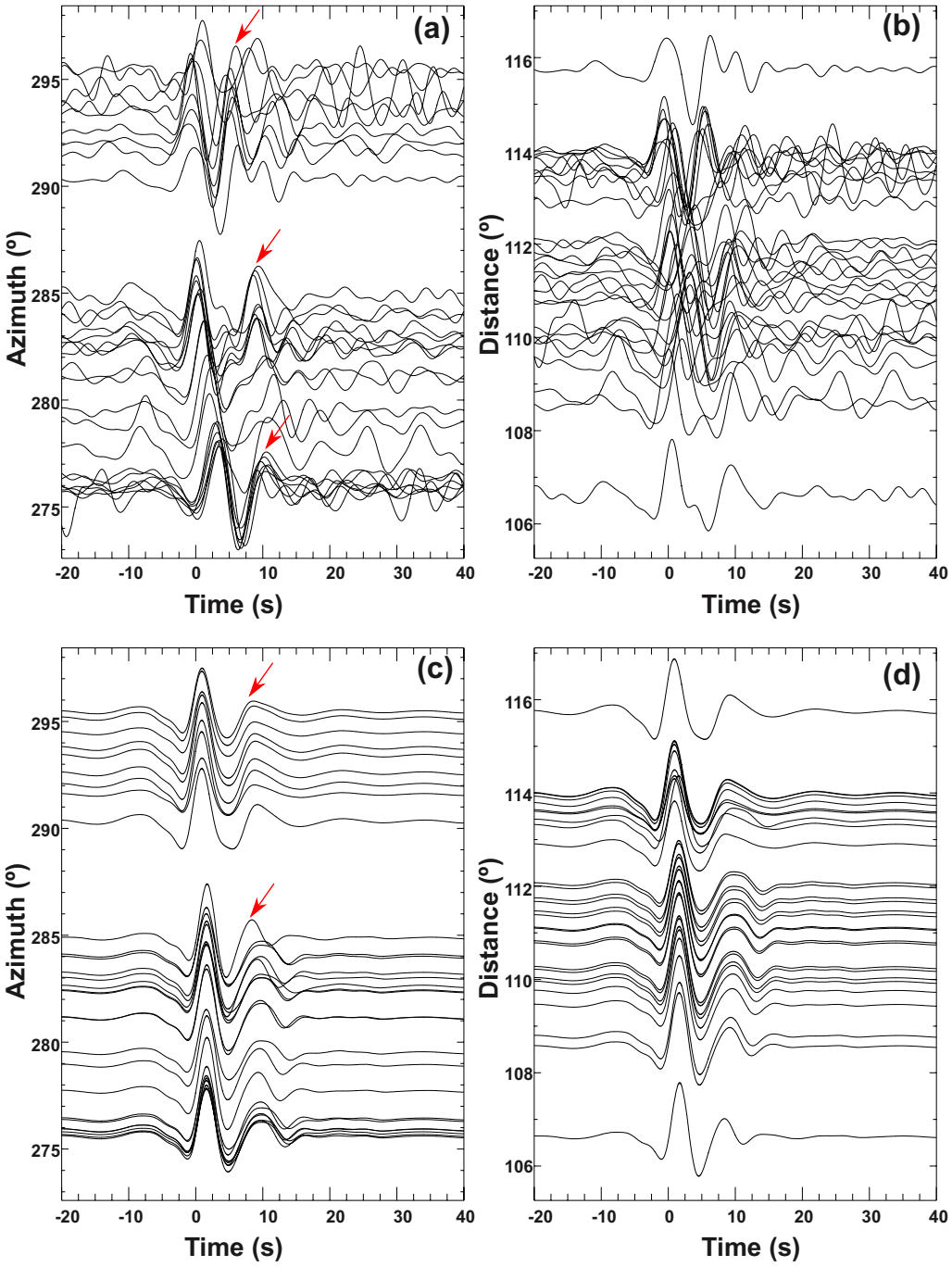

Figure 2. Velocity waveforms recorded by the Indian network for the event D (shown in Fig. 1) from the Fiji–Tonga slab. The waveforms are plotted in terms of (a) azimuth and (b) distance. The horizontal axis is the time relative to the synthetic arrival time of the SH_{diff} phase computed using the PREM model (Dziewonski & Anderson 1981). The red arrow marks the second pulse. Synthetic seismograms for our preferred model are also plotted in terms of (c) azimuth and (d) distance.

Table 1. List of earthquakes that show clear secondary pulses after the SH_{diff} phases. These earthquakes are assigned an alphabetic event name.

E_date	E_time (s)	E_lat. (°)	E_long. (°)	E_depth (km)	Mag.	Remark
10/16/2007	21:05:46.800	−25.700	179.720	512.40	6.6	Event A
11/09/2009	10:45:03.400	−17.110	178.530	603.90	7.3	Event B
02/21/2011	10:57:57.600	−25.950	178.470	567.50	6.6	Event C
04/28/2012	10:08:12.700	−18.790	−174.260	140.70	6.7	Event D
09/24/2016	21:28:48.300	−19.810	−178.160	610.30	6.9	Event E

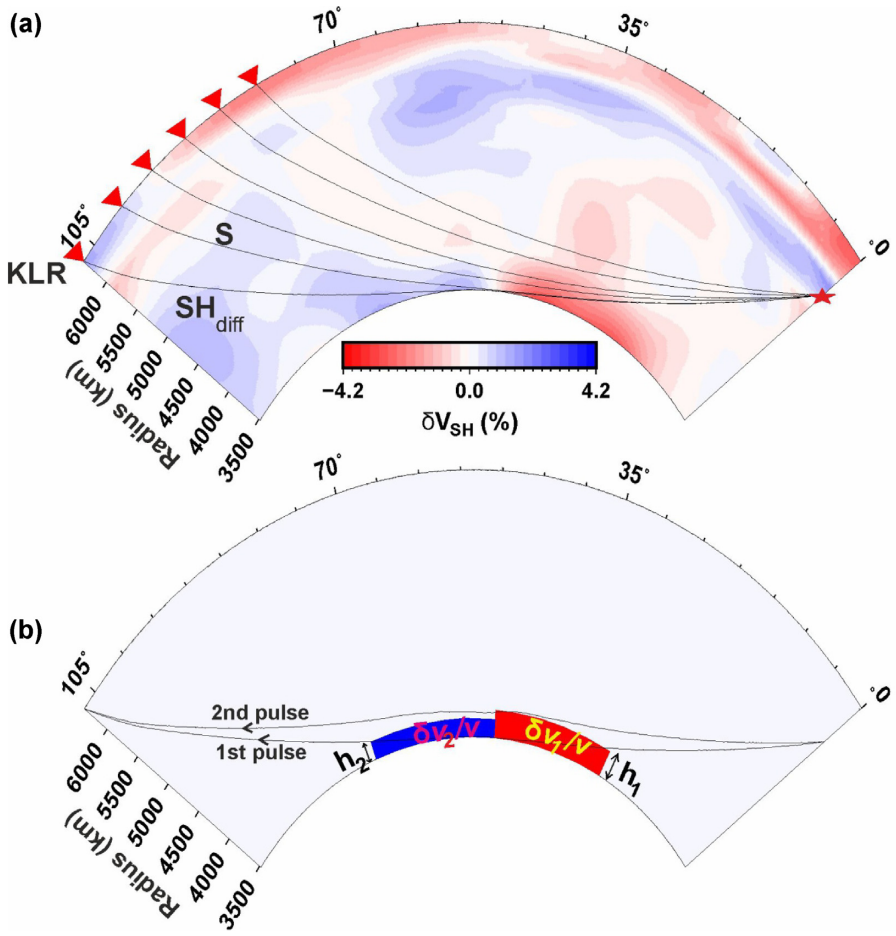

Figure 3. (a) Depth section of the shear wave tomographic velocity model (Takeuchi 2012) including the event B and station KLR. The $SH_{\rm diff}$ ray path for event B and station KLR (shown in Fig. 1) and direct S ray paths for epicentral distance between 80° and 100° computed using PREM (Dziewonski & Anderson 1981) are shown. (b) The two-dimensional model considered in this study together with the definition of model parameters. h_1, $\delta v_1/v$ and h_2, $\delta v_2/v$ represent the thickness and shear velocity perturbation for the first and second heterogeneous block, respectively. b° denotes the boundary location, which is measured in terms of the distance from the epicentre of event B. Schematic ray paths of the first and second pulses are also shown. The preferred values of the model parameters can vary between the northern array and the southern array; $h_1 = 200$ km, $h_2 = 200$ km, $\delta v_1/v = 1.5$ per cent, $\delta v_2/v = 1$ per cent, $b^\circ = 49^\circ$ for the northern array and $h_1 = 300$ km, $h_2 = 200$ km, $\delta v_1/v = 1.5$ per cent, $\delta v_2/v = 1$ per cent, $b^\circ = 49^\circ$ for the southern array, respectively.

discuss the azimuthal dependence. We approximated the heterogeneous structures shown in Fig. 3(a) by a 2-D model illustrated in Fig. 3(b). The modelling is performed using the spectral-element code AxiSEM that simulates a 3-D wavefield for an axisymmetric spherical model (Nissen-Meyer *et al.* 2014). Models for both the northern and southern arrays are azimuthally homogeneous and defined in terms of the cross-section including event B. The location of the other events and stations is appropriately projected on the defined cross-sections. The heterogeneities are approximated by lower velocity and higher velocity blocks (illustrated by the red and blue boxes in Fig. 3b), and the rest of the regions are assumed to be laterally homogeneous. Readers might think that the model configuration assumed in Fig. 3(b) appears to be slightly ad hoc; however, we think it is sufficiently justified. The boundary between the lower and higher velocity anomalies is assumed to be sharp, but it is consistent with the findings of Idehara *et al.* (2013), who suggested an abrupt change in *ScS* traveltimes with less than 500 km of transition zone. The top surface of the LLSVP is assumed to be horizontal, but we confirmed by numerical simulation that the presence of a large-amplitude topography (>∼200 km) with scale length comparable to the whole of our study region is unlikely because the direct *S* ray path quasi-parallel to the CMB and the top of the LLSVP results in its refraction (or diffraction) and arrival as a secondary pulse adjacent to the $SH_{\rm diff}$ phase.

We define the following five model parameters (Fig. 3): the height of the lower and higher velocity blocks (denoted by h_1 and h_2, respectively), their volumetric velocity perturbations (denoted by $\delta v_1/v$ and $\delta v_2/v$, respectively, where v is the velocity of the spherically symmetric reference model, PREM; Dziewonski & Anderson 1981) and the boundary location (denoted by b°, which is the angular distance from event B). We determine the optimal parameters to explain the phases recorded by the northern and southern arrays.

4.1 Model inference

Synthetic traveltimes are evaluated using synthetic seismograms computed for the source–receiver geometries in our data set. We assumed a point source with a Gaussian source time function having a dominant period of 3.2 s. However, because the effects of anelasticity prevail, the resultant synthetic seismograms are essentially identical to those computed for a delta function. The temporary grid interval used in the computations is 0.025 s, which is sufficiently small compared to the dominant period. After comparing

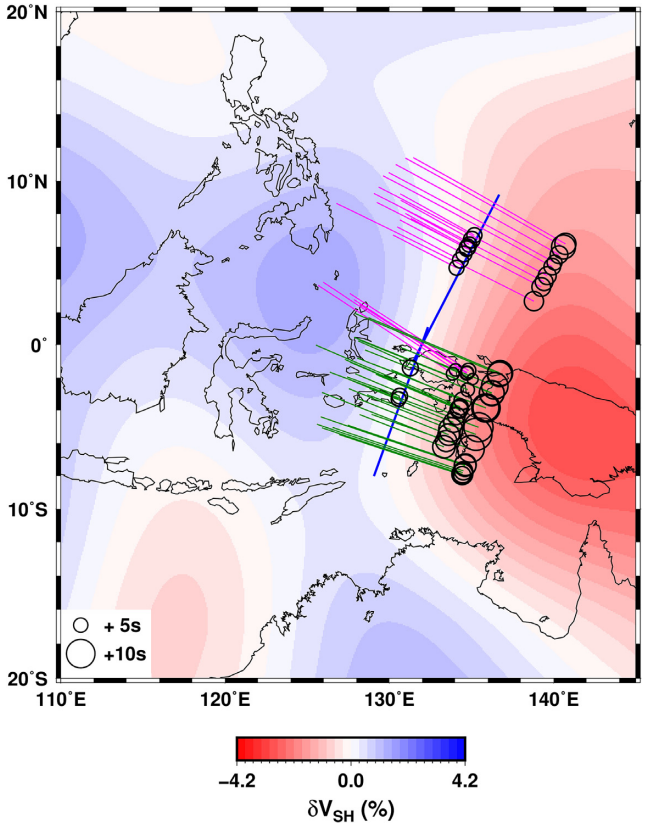

Figure 4. Traveltime residuals (black circles) projected at the entry point of the $SH_{\rm diff}$ ray path to the CMB. The magenta and dark green lines represent the ray segment of $SH_{\rm diff}$ on the CMB for the northern and southern seismic array, respectively. The background colour represents the tomographic shear velocity model of Takeuchi (2012).

synthetic seismograms computed using PREM with the observed waveforms corresponding to the selected events, we found that the pulse width in the synthetic seismograms is systematically broader than the observations. We therefore tuned the anelasticity factor Q_s in the PREM, by tripling the Q_s value in the lower mantle (i.e. we used $Q_s = 936$). We also found that the synthetic seismograms are more severely contaminated by crustal reverberations than the observed waveforms. Therefore, we replaced the Moho discontinuity with a smooth one. Using synthetic seismograms, the synthetic relative traveltime between the first and second phase is measured in the same way as done for the observed data. The above modifications of the model will not significantly affect the measurements of differential traveltimes. In view of the trade-off among model parameters (h_1, h_2, $\delta v_1/v$, $\delta v_2/v$ and b°), we fixed three parameters (h_2, $\delta v_2/v$ and b°) to appropriate values and searched for the optimal values of h_1 and $\delta v_1/v$ for the northern and southern array, respectively. We fixed $b^\circ = 49^\circ$ at the location shown by the dark blue lines in Fig. 4, referring to the tomography model of Takeuchi (2012). Based on this tomography model, we also assumed $h_2 = 200$ km and $\delta v_2/v = 1$ per cent.

The choice of these values is justified below. The boundary location ($b^\circ = 49^\circ$) is almost consistent (within an accuracy of $\sim 3^\circ$) among various tomography models (e.g. Houser *et al.* 2008; Simmons *et al.* 2010; Koelemeijer *et al.* 2016). All these tomography models show slightly higher velocity anomalies ($<\sim 1$ per cent) to the west of this boundary, which is also consistent with our assumed model ($\delta v_2/v = 1$ per cent). Traveltimes of *ScS* reflections from this region also suggest slightly higher velocity anomalies (e.g. Houser *et al.* 2008; Idehara *et al.* 2013), and the absolute values of residuals are generally moderate/small ($<\sim 4s$), around half of that for the phases reflected in the lower velocity region of our study area. We chose the appropriate values of h_2 and $\delta v_2/v$ from the tomography model of Takeuchi (2012) but the values ($h_2 = 200$ km and $\delta v_2/v = 1$ per cent) are consistent with the *ScS* observations by Houser *et al.* (2008) and Idehara *et al.* (2013).

Figs 6(a) and (b) show a comparison between the observed and synthetic differential traveltimes of the southern array for various pairs of h_1 and $\delta v_1/v$. To quantitatively confirm the consistency between the observation and the synthetics, we also modelled the traveltimes picked from the synthetic seismograms (shown by black pluses), by a regression line in a fashion similar to that in Fig. 5. If the thickness of the LLSVP increases or decreases, then the relative apparent velocity (i.e. the slope of the regression line) increases or decreases, respectively (Fig. 6a). In contrast, this velocity is not very sensitive to the volumetric velocity perturbation of the LLSVP, $\delta v_1/v$ (compare Figs 6a and b). This is probably because, although the model is two-dimensional, the apparent velocity of the first and second pulses primarily reflects the velocity at the bottoming points: mantle velocities at the bottom and at the top of the LLSVP (note that the bottoming point of the secondary pulse is below the top of the LLSVP. However, considering the grazing features of the ray path, we can assume that the velocity at the bottoming point is essentially equal to that at the top of the LLSVP). From a comparison of Figs 6(a) and (b), we concluded that $h_1 = 300$ km is optimal for the southern array.

Figs 6(c) and (d) show the residuals between the observed and synthetic absolute traveltimes of the first pulse of the southern array for various pairs of h_1 and $\delta v_1/v$. The average residuals and their standard deviations are also shown in each figure. Because our data set of differential traveltimes does not constrain the volumetric heterogeneity very well (Figs 6a and b), we also refer to the absolute time. The primary problem related to the use of absolute arrival times is that the data are affected by heterogeneity not only in the lowermost mantle but also in other parts of the mantle. We therefore use the tomography model of Takeuchi (2012) to subtract the traveltime residuals resulting from heterogeneities in the mantle, which are greater than 300 km from the CMB. The corrected residuals are plotted as brown pluses in Figs 6(c) and (d). However, it can be seen that the mantle corrections do not cause any systematic bias. From these comparisons, we concluded that $\delta v_1/v = -1.5$ per cent is optimal for the southern array.

Similarly, for the northern array, the model parameters $h_1 = 200$ km and $\delta v_1/v = -1.5$ per cent explain the traveltime observations (Figs 5a and 7). However, for the northern array data, the mantle corrections are rather systematic (Fig. 7b), probably because of higher velocities in the upper mantle beneath it. We therefore need to admit larger uncertainties for the volumetric heterogeneity ($\delta v_1/v$) of the northern region. However, we can well constrain the thickness h_1 from the relative apparent velocity that is insensitive to receiver- and source-side structures, and can conclude that azimuthal variation of topography is a robust component of our model.

In summary, our preferred model for the southern array is $h_1 = 300$ km and $\delta v_1/v = -1.5$ per cent, which produces traveltimes resembling the observed ones (Figs 5b and 6). Our preferred model for the northern array is $h_1 = 200$ km and $\delta v_1/v = -1.5$ per cent, which explains the observations (Figs 5a and 7). Although these preferred parameters are inferred from traveltimes, the resultant synthetic seismograms show a satisfactory agreement with the observed waveforms (Fig. 2).

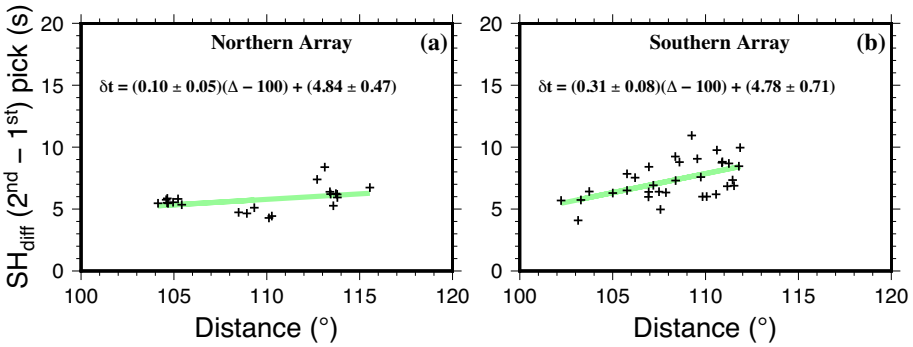

Figure 5. The observed differential traveltimes (black pluses) between the second and first pulses as a function of distance for the (a) northern and (b) southern seismic array, respectively. The green colour bar represents the regression fit. The numerical expressions of δt (in the inset) represent the explicit equations of the regression line along with their uncertainties. Δ denotes the distance in degrees.

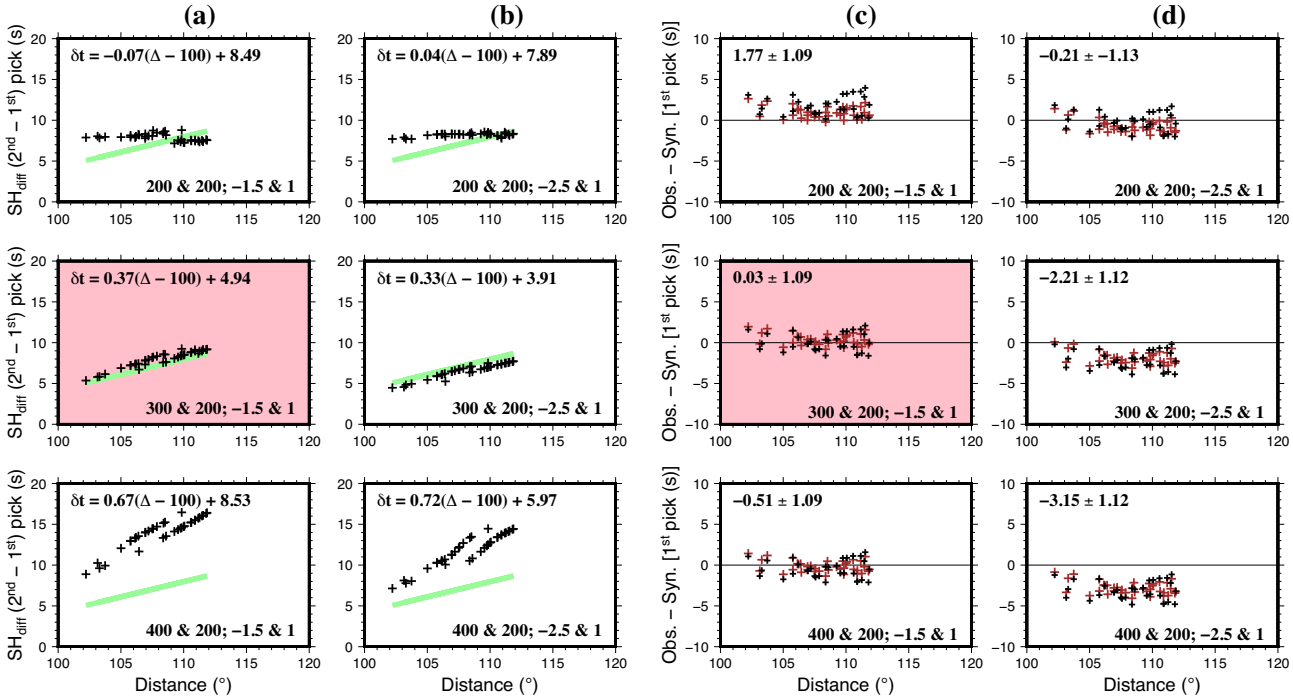

Figure 6. (a) Synthetic differential traveltimes (black pluses) for the stations in the southern array calculated using PREM (Dziewonski & Anderson 1981) for $\delta v_1/v = -1.5$ per cent and $h_1 = 200$ km (top), $h_1 = 300$ km (centre), and $h_1 = 400$ km (bottom). The green bar represents the regression fit of observed data for the southern array. The numerical expressions of δt (in the inset) represent the explicit equations of the regression line for the synthetic traveltimes. Δ denotes the distance in degrees. (b) Same as (a) for $\delta v_1/v = -2.5$ per cent. (c) The traveltime residuals of the first pulse (pluses) for the models with $\delta v_1/v = -1.5$ per cent and $h_1 = 200$ km (top), $h_1 = 300$ km (centre), and $h_1 = 400$ km (bottom). The black and brown pluses denote the residuals without and with the corrections for heterogeneities in the mantle, except for the lowermost 300 km region. The numerical values in the top inset represent the average and standard deviation of the residuals uncorrected for heterogeneities. (d) The same as (c) except for cases with $\delta v_1/v = -2.5$ per cent. In all the plots, we assume $\delta v_2/v = 1.0$ per cent, $h_2 = 200$ km, and $b^\circ = 49^\circ$. The pink fill represents the selected model for the southern array.

4.2 Effects of uncertainties in the assumed models

Our derivation of the optimal models is based on the assumption of the values of three parameters (h_2, $\delta v_2/v$ and b°). Of course, there are uncertainties in the assumed values, and we need to understand how they affect the waveforms and thus bias our inference of h_1 and $\delta v_1/v$. The boundary location (b°) is primarily sensitive to the amplitude of the secondary pulse and does not affect the traveltimes. When the boundary is shifted 3° towards the east/west, the amplitude of the second pulse decreases/increases. For our preferred model with the boundary location $b^\circ = 49^\circ$, the amplitude of the secondary pulse in the synthetic seismogram is $\sim 2.7 - 15.8$ per cent of that of the first pulse, whereas for the model with the boundary located at $b^\circ = 46^\circ$, it is $\sim 2.6 - 9.2$ per cent (Supporting Information Fig. S3). However, considering that the focusing effects cannot be modelled by our 2-D simulation, we did not use detailed amplitude information to constrain the model. The volumetric heterogeneity ($\delta v_2/v$) is primarily sensitive to the arrival times of the first pulse, while the thickness of the higher velocity anomalies (h_2) does not much affect the waveforms, as long as it is confined to the lowermost 200 km (or as long as its height is smaller than that of the LLSVP). Therefore, the uncertainties in h_2 do not affect much, but the uncertainties in $\delta v_2/v$ should have some trade-off with our inference of $\delta v_1/v$. However, we do not think that the assumed uncertainty in $\delta v_2/v$ is large.

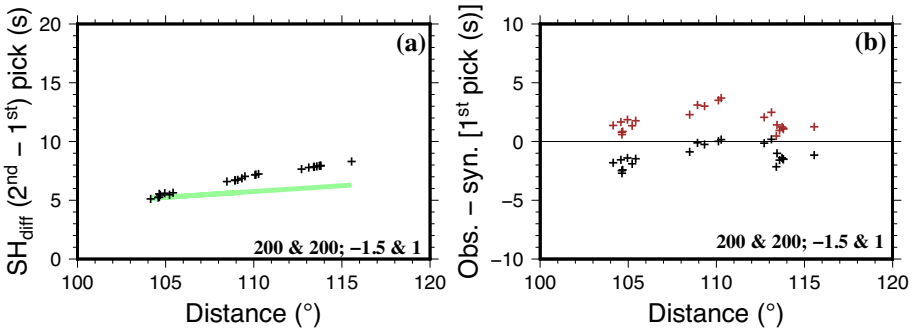

Figure 7. (a) Synthetic differential traveltimes (black pluses) for the stations in the northern array calculated using our preferred model. The green bar represents the regression fit of the observed data for the northern array. (b) The same as Fig. 6(c) (top) for the residuals from the northern array.

We can therefore conclude that our inference on the variation in the inferred h_1 is robust.

5 DISCUSSION

In this study, we showed that the observed waveforms can be explained without much alteration of the existing tomography models. Our observations suggest that the western edge of the Pacific LLSVP extends in the NE–SW direction from 129.5°E to 136.5°E and has a smaller scale topography. There is a variation in the topography of the western edge of the Pacific LLSVP from 300 km to 200 km, from south to north. The observations also suggest that the edge of the LLSVP (i.e. our study region) has both significant thickness and surface topography, which favour the LLSVP to be a chemically distinct pile. The existence of topography whose scale length is much smaller than that of the whole Pacific LLSVP suggests some dynamic process at the western edge, such as a regional plume, instability of a dome-like structure or push due to downwelling from the outside (e.g. Tan & Gurnis 2007; Tan *et al.* 2011).

The sharpness of the top of the LLSVP is important to constrain the origin of this large anomaly. We consider the same model as in Fig. 3(b), except for the blurred top of the low-velocity region, with a transition zone of up to 70 km thickness. The amplitude of the secondary phase decreases if the thickness of the transition zone is greater than ∼60 km (Supporting Information Fig. S4). Although precise quantification is difficult, considering the observed amplitudes of the secondary pulses are more than ∼30 per cent of the first pulse for most of the cases (see Fig. 2 and Supporting Information Fig. S2), a gradual transition from the ambient mantle to the LLSVP is unlikely and the LLSVP should be a distinct region.

It is debated whether the origin of the LLSVP is thermal or chemical (e.g. McNamara & Zhong 2005; Bull *et al.* 2009; Davies *et al.* 2012). Our results favour a chemical origin because of the following reasons. If the thermal anomalies were the origin, we expect predominance of smaller scale anomalies with a complex geometry composed of plume clusters (e.g. Davies *et al.* 2012). Such smaller scale features (<100 km) were required to explain the sharp sides inferred from previous seismological studies (e.g. Ni *et al.* 2002; To *et al.* 2005; Sun *et al.* 2009). However, to explain the secondary pulses observed in this study, we need a quasi-horizontal upper boundary of the lower velocity region (such as that shown in Fig. 3b); otherwise we hardly expect phases with similar apparent velocity and arrival time as those for the SH_{diff} phase. To further constrain the origin, we probably need to analyse P_{diff} and its post- or pre-cursors, which is a future research topic.

Finally, we show the discrepancies between our preferred model and previous regional models, and discuss possible reasons for them. Idehara *et al.* (2013) previously studied a region similar to our study region. They used *ScS* phases propagating in the N–S and E–W directions. The *ScS* data in the E–W direction has an azimuthal coverage similar to our data from the northern array. Their model has a 250-km-thick LLSVP with −1.5 per cent velocity reduction, bounded at 137°E with a +1.0 per cent higher velocity region, which is 250 km thick, while our model for the northern array has a 200-km-thick LLSVP with −1.5 per cent velocity reduction, bounded around 136.5°E with a +1.0 per cent higher velocity region. Our model is close to the model of Idehara *et al.* (2013), but has marginal discrepancies. We think it is, at least, partly due to the assumption in Idehara *et al.* (2013) that the boundary should be precisely in the N–S direction. Indeed, the boundary locations suggested by the N–S and E–W data of Idehara *et al.* (2013) are not very consistent with each other (see fig. 3c of Idehara *et al.* 2013). Furthermore, the residuals for the longitude range 126°E to 140°E are highly scattered (see their fig. 2b). It appears that the ScS reflections sampling the northern part of their study region between 126°E and 135°E (which is in the higher velocity region in their model) systematically show delayed arrivals, which may be interpreted as a consequence of the inappropriate boundary direction assumed in Idehara *et al.* (2013). The boundary direction and location of our model are generally consistent with the result of He & Wen (2012), who studied ScS traveltimes sampling the Pacific LLSVP and its adjacent regions. Although the boundary location of He & Wen (2012) is slightly eastward of our boundary, the difference is within the uncertainty limits. The fact that the higher velocity anomalies adjacent to the LLSVP were not considered in He & Wen (2012) may be partly contributing to the discrepancy.

6 CONCLUSIONS

The waveforms of five deep earthquakes from the Fiji–Tonga subduction zone recorded by a seismic array in India reveal a secondary pulse just after the SH_{diff} phase. The second pulse is suggested to be generated by multipathing of *S* waves due to the LLSVP atop the core–mantle boundary. The traveltime difference between the second and first pulse together with their differential apparent velocity can be used to retrieve information on the azimuthal variations of the thickness at the western edge of the Pacific LLSVP. Forward modelling suggests that the western boundary of the Pacific LLSVP is oriented in the NE–SW direction and the thickness of the Pacific LLSVP varies from 300 km to 200 km from south to north. The observation favours the LLSVP to be a chemically distinct pile with

significant surface topography whose overall geometry is dome-like rather than sandpile-like.

ACKNOWLEDGEMENTS

SKR is thankful to the Director, NGRI, for his support during the work carried out at the Earthquake Research Institute (ERI), University of Tokyo, and for his permission to publish the work. SKR is thankful to Xin Long for his help in running the AxiSEM code. We sincerely thank the Editor and reviewers for their constructive comments that improved the quality of the manuscript. Waveform data used in this study can be obtained by sending a mail to the Director (director@ngri.res.in), CSIR-NGRI, Hyderabad. The Council of Scientific and Industrial Research (CSIR) and the Ministry of Earth Sciences (MoES) are gratefully acknowledged for funding the projects in the Indian seismic array. Plots are generated using the Generic Mapping Tools (GMT). This research is partly supported by JSPS KAKENHI Grant Number JP15H05832.

REFERENCES

Becker, T.W. & Boschi, L., 2002. A comparison of tomographic and geodynamic mantle models, *Geochem. Geophys. Geosyst.,* **3,** doi:10.1029/2001GC000168.

Bull, A.L., McNamara, A.K. & Ritsema, J., 2009. Synthetic tomography of plume cluster and thermochemical piles, *Earth planet. Sci. Lett.,* **278,** 152–162.

Cottaar, S. & Romanowicz, B., 2013. Observations of changing anisotropy across the southern margin of the African LLSVP, *Geophys. J. Int.,* **195**(2), 1184–1195.

Creasy, N., Long, M.D. & Ford, H.A., 2017. Deformation in the lowermost mantle beneath Australia from observations and models of seismic anisotropy, *J. geophys. Res.,* **122**(7), 5243–5267.

Davaille, A., 1999. Simultaneous generation of hotspots and superswells by convection in a heterogeneous planetary mantle, *Nature,* **402,** 756–760.

Davies, D.R., Goes, S., Davies, J., Schuberth, B., Bunge, H.-P. & Ritsema, J., 2012. Reconciling dynamic and seismic models of Earth's lower mantle: the dominant role of thermal heterogeneity, *Earth planet. Sci. Lett.,* **353–354,** 253–269.

Dziewonski, A.M., 1984. Mapping the lower mantle: determination of lateral heterogeneity in P velocity up to degree and order 6, *J. geophys. Res.,* **89**(B7), 5929–5952.

Dziewonski, A.M. & Anderson, D.L., 1981. Preliminary reference earth model, *Phys. Earth planet. Inter.,* **25**(4), 297–356.

Ford, H.A., Long, M.D., He, X. & Lynner, C., 2015. Lowermost mantle flow at the eastern edge of the African Large Low Shear Velocity Province, *Earth planet. Sci. Lett.,* **420,** 12–22.

French, S.W. & Romanowicz, B.A., 2014. Whole-mantle radially anisotropic shear velocity structure from spectral-element waveform tomography, *Geophys. J. Int.,* **199,** 1303–1327.

Frost, D.A. & Rost, S., 2014. The *P*-wave boundary of the Large-Low Shear Velocity Province beneath the Pacific, *Earth planet. Sci. Lett.,* **403,** 380–392.

Garnero, E.J., 2000. Heterogeneity of the lowermost mantle, *Annu. Rev. Earth Planet. Sci.,* **28,** 509–537.

He, Y. & Wen, L., 2009. Structural features and shear-velocity structure of the 'Pacific anomaly', *J. geophys. Res.,* **114,** B02309.

He, Y. & Wen, L., 2012. Geographic boundary of the 'Pacific anomaly' and its geometry and transitional structure in the north, *J. geophys. Res.,* **117,** B09308.

He, Y., Wen, L. & Zheng, T., 2006. Geographic boundary and shear wave velocity structure of the 'Pacific anomaly' near the core–mantle boundary beneath western Pacific, *Earth planet. Sci. Lett.,* **244**(1), 302–314.

Houser, C., Masters, G., Shearer, P. & Laske, G., 2008. Shear and compressional velocity models of the mantle from cluster analysis of long-period waveforms, *Geophys. J. Int.,* **174**(1), 195–212.

Idehara, K., Tanaka, S. & Takeuchi, N., 2013. High-velocity anomaly adjacent to the western edge of the Pacific low-velocity province, *Geophys. J. Int.,* **192**(1), 1–6.

Ishii, M. & Tromp, J., 1999. Normal-mode and free-air gravity constraints on lateral variations in velocity and density of Earth's mantle, *Science,* **285**(5431), 1231–1236.

Kendall, J.-M. & Silver, P.G., 1996. Constraints from seismic anisotropy on the nature of the lower mantle, *Nature,* **381,** 409–412.

Koelemeijer, P., Ritsema, J., Deuss, A. & van Heijst, H.-J., 2016. SP12RTS: a degree-12 model of shear- and compressional-wave velocity for Earth's mantle, *Geophys. J. Int.,* **204**(2), 1024–1039.

Lekic, V., Cottaar, S., Dziewonski, A. & Romanowicz, B., 2012. Cluster analysis of global lower mantle tomography: a new class of structure and implications for chemical heterogeneity, *Earth planet. Sci. Lett.,* **357–358,** 68–77.

Long, M.D. & Lynner, C., 2015. Seismic anisotropy in the lowermost mantle near the Perm Anomaly, *Geophys. Res. Lett.,* **42,** 7073–7080.

Lynner, C. & Long, M.D., 2014. Lowermost mantle anisotropy and deformation along the boundary of the African LLSVP, *Geophys. Res. Lett.,* **41,** 3447–3454.

Masters, G., Laske, G., Bolton, H. & Dziewonski, A.M., 2000. The relative behavior of shear velocity, bulk sound speed, and compressional velocity in the mantle: implications for chemical and thermal structure, in *Earth's Deep Interior: Mineral Physics and Tomography From the Atomic to the Global Scale,* Vol. **117,** pp. 63–87, eds Karato, S., Forte, A., Liebermann, R., Masters, G. & Stixrude, L., American Geophysical Union.

McNamara, A.K. & Zhong, S., 2005. Thermochemical structures beneath Africa and the Pacific Ocean, *Nature,* **437,** 1136–1139.

Murakami, M., Hirose, K., Kawamura, K., Sata, N. & Ohishi, Y., 2004. Post-perovskite phase transition in mgsio3, *Science,* **304**(5672), 855–858.

Ni, S. & Helmberger, D.V., 2003. Ridge-like lower mantle structure beneath South Africa, *J. geophys. Res.,* **108**(B2), doi: 10.1029/2001JB001545.

Ni, S., Tan, E., Gurnis, M. & Helmberger, D., 2002. Sharp sides to the African superplume, *Science,* **296**(5574), 1850–1852.

Nissen-Meyer, T., van Driel, M., Stähler, S.C., Hosseini, K., Hempel, S., Auer, L., Colombi, A. & Fournier, A., 2014. AxiSEM: broadband 3-D seismic wavefields in axisymmetric media, *Solid Earth,* **5**(1), 425–445.

Rao, B.P. & Kumar, M.R., 2014. Seismic evidence for slab graveyards atop the core–mantle boundary beneath the Indian Ocean geoid low, *Phys. Earth planet. Inter.,* **236,** 52–59.

Ritsema, J., Ni, S., Helmberger, D.V. & Crotwell, H.P., 1998. Evidence for strong shear velocity reductions and velocity gradients in the lower mantle beneath Africa, *Geophys. Res. Lett.,* **25**(23), 4245–4248.

Ritsema, J., van Heijst, H.J. & Woodhouse, J.H., 1999. Complex shear wave velocity structure imaged beneath Africa and Iceland, *Science,* **286**(5446), 1925–1928.

Roy, S.K., Srinagesh, D., Saikia, D., Singh, A. & Kumar, M.R., 2012. Seismic anisotropy beneath the eastern dharwar craton, *Lithosphere,* **4**(4), 259–268.

Roy, S.K., Kumar, M.R. & Srinagesh, D., 2014. Upper and lower mantle anisotropy inferred from comprehensive SKS and SKKS splitting measurements from India, *Earth planet. Sci. Lett.,* **392,** 192–206.

Roy, S.K., Kumar, M.R., Rao, Y.B., Srijayanthi, G., Srinagesh, D., Satyanarayana, H. & Sarkar, D., 2016. Imprints of diverse mantle deformational episodes in the Cauvery suture zone, South India, *Precambrian Res.,* **278,** 207–217.

Schubert, G., Masters, G., Olson, P. & Tackley, P., 2004. Superplumes or plume clusters? *Phys. Earth planet. Inter.,* **146**(1), 147–162.

Simmons, N.A., Forte, A.M., Boschi, L. & Grand, S.P., 2010. Gypsum: a joint tomographic model of mantle density and seismic wave speeds, *J. geophys. Res.,* **115,** B12310.

Su, W. & Dziewonski, A.M., 1991. Predominance of long-wavelength heterogeneity in the mantle, *Nature,* **352,** 121–126.

Su, W. & Dziewonski, A.M., 1997. Simultaneous inversion for 3-D variations in shear and bulk velocity in the mantle, *Phys. Earth planet. Inter.,* **100**(1), 135–156.

Sun, D. & Miller, M.S., 2013. Study of the western edge of the African large low shear velocity province, *Geochem. Geophys. Geosyst.,* **14**(8), 3109–3125.

Sun, D., Helmberger, D., Ni, S. & Bower, D., 2009. Direct measures of lateral velocity variation in the deep Earth, *J. geophys. Res.,* **114,** B05303, doi: 10.1029/2008JB005873.

Tackley, P.J., 2002. Strong heterogeneity caused by deep mantle layering, *Geochem. Geophys. Geosyst.,* **3**(4), 1–22.

Tackley, P.J., 2013. *Three-Dimensional Simulations of Mantle Convection with a Thermo-Chemical Basal Boundary Layer: D"?,* pp. 231–253, American Geophysical Union.

Takeuchi, N., 2007. Whole mantle SH velocity model constrained by waveform inversion based on three-dimensional Born kernels, *Geophys. J. Int.,* **169,** 1153–1163.

Takeuchi, N., 2012. Detection of ridge-like structures in the Pacific Large Low-Shear-Velocity Province, *Earth planet. Sci. Lett.,* **319–320,** 55–64.

Takeuchi, N. & Obara, K., 2010. Fine-scale topography of the D" discontinuity and its correlation to volumetric velocity fluctuations, *Phys. Earth planet. Inter.,* **183,** 126–135.

Takeuchi, N., Morita, Y., Xuyen, N.D. & Zung, N.Q., 2008. Extent of the low-velocity region in the lowermost mantle beneath the western Pacific detected by the Vietnamese Broadband Seismograph Array, *Geophys. Res. Lett.,* **35**(5), 1–5.

Tan, E. & Gurnis, M., 2005. Metastable superplumes and mantle compressibility, *Geophys. Res. Lett.,* **32**(20), L20307.

Tan, E. & Gurnis, M., 2007. Compressible thermochemical convection and application to lower mantle structures, *J. geophys. Res.,* **112**(B6), doi: 10.1029/2006JB004505.

Tan, E., Leng, W., Zhong, S. & Gurnis, M., 2011. On the location of plumes and lateral movement of thermochemical structures with high bulk modulus in the 3-D compressible mantle, *Geochem. Geophys. Geosyst.,* **12**(7), doi: 10.1029/2011GC003665.

Tanaka, S., Kawakatsu, H., Obayashi, M., Chen, Y.J., Ning, J., Grand, S.P., Niu, F. & Ni, J., 2015. Rapid lateral variation of P-wave velocity at the base of the mantle near the edge of the Large-Low Shear Velocity Province beneath the western Pacific, *Geophys. J. Int.,* **200**(2), 1052–1065.

Tanimoto, T., 1990. Long-wavelength s-wave velocity structure throughout the mantle, *Geophys. J. Int.,* **100**(3), 327–336.

To, A., Romanowicz, B., Capdeville, Y. & Takeuchi, N., 2005. 3D effects of sharp boundaries at the borders of the African and Pacific superplumes: observation and modeling, *Earth planet. Sci. Lett.,* **233**(1), 137–153.

Trampert, J., Deschamps, F., Resovsky, J. & Yuen, D., 2004. Probabilistic tomography maps chemical heterogeneities throughout the lower mantle, *Science,* **306**(5697), 853–856.

Wang, Y. & Wen, L., 2007. Geometry and P and S velocity structure of the 'African Anomaly', *J. geophys. Res.,* **112,** B05313, doi: 10.1029/2006JB004483.

Woodward, R.L. & Masters, G., 1991. Lower-mantle structure from ScS-S differential travel times, *Nature,* **352,** 231–233.

Zhao, C., Garnero, E.J., McNamara, A.K., Schmerr, N. & Carlson, R.W., 2015. Seismic evidence for a chemically distinct thermochemical reservoir in Earth's deep mantle beneath Hawaii, *Earth planet. Sci. Lett.,* **426,** 143–153.

SUPPORTING INFORMATION

Supplementary data are available at *GJI* online.

Table S1. The seismic stations used in this study. Stations are categorized into northern and southern arrays according to the station latitude greater and less than 22°, respectively.

Figure S1. (a) The cartoon shows the ray path of the direct *SH* and SH_{diff} wave in the presence of the LVZ above the CMB. Traveltime curves of *SH* (black), *ScS* (blue) and SH_{diff} (brown) for (b) the PREM model and (c) the Prem model with a velocity reduction of −1.5 per cent for 300 km above CMB. The event depth is assumed to be 140.7 km.

Figure S2. Displacement waveform for the event A–E from the Fiji–Tonga slab. (a) *SH* phase recorded by station KKM in SE Asia. The epicentral distance and azimuth for station KKM are 65.7° and 284.9°, respectively, from event B. The SH_{diff} waveform recorded by the Indian network is plotted in terms of (b) azimuth and (c) distance.

Figure S3. (a) Synthetic velocity waveforms for event B (shown in Fig. 1) and our preferred model ($b° = 49°$). (b) The same as (a) except for computing synthetics for the models with shifting the boundary location to 46°.

Figure S4. Synthetic velocity waveforms at the epicentral distance of 115° for event B. The magenta waveform is for our preferred model with the sharp top of the lower velocity region in Fig. 3(b). The other waveforms are also computed for our preferred model except for having a transition zone with various thicknesses (in the inset) at the top of the lower velocity region.

Please note: Oxford University Press is not responsible for the content or functionality of any supporting materials supplied by the authors. Any queries (other than missing material) should be directed to the corresponding author for the paper.